Interfacial Pathways in $Na_2B_{12}H_{12}/SiO_2$ Nanocomposites Boost the Ionic Conductivity and Enable Solid-State Sodium Batteries at Room Temperature

Jonas D. Hehn[a], Gabriele Masia[a,b], Masoud Lazemi[a], Juliette C. Verschoor[a], Karan Kotalgi[a], Savannah J. Turner[c], Hlynur Gretarsson[d], Martin Sundermann[d,e], Fabrizio Murgia[b], Petra E. de Jongh[a] and Peter Ngene[a]*

[a] *Materials Chemistry and Catalysis, Debye Institute for Nanomaterials Science, Utrecht University, 3584 CG Utrecht, The Netherlands*

[b] *Department of Chemical, Physical, Mathematical and Natural Sciences, University of Sassari, 07100 Sassari, Italy*

[c] *Electron Microscopy Centre, Utrecht University, 3584 CG Utrecht, The Netherlands*

[d] *Deutsches Elektronen-Synchrotron DESY, 22607 Hamburg, Germany*

[e] *Max Planck Institute for Chemical Physics of Solids, 01187 Dresden, Germany*

* Corresponding author E-mail: p.ngene@uu.nl

Table S1. Overview of all sample compositions and properties.

Volume % SiO_2	Weight % SiO_2	Weight % $Na_2B_{12}H_{12}$	SiO_2 type	Ball milling duration
25	38.1	61.9	Aerosil 380	4
35	49.8	50.2	Aerosil 380	1
35	49.8	50.2	Aerosil 380	2
35	49.8	50.2	Aerosil 380	3
35	49.8	50.2	Aerosil 380	3.5
35	49.8	50.2	Aerosil 380	4
35	49.8	50.2	Aerosil 380	8
40	55.2	44.8	Aerosil 380	4
50	64.9	35.1	Aerosil 380	4
75	84.7	15.3	Aerosil 380	4
35	49.8	50.2	Aerosil 90	4
35	49.8	50.2	Aerosil 200	4
35	49.8	50.2	Aerosil 300	4
35	49.8	50.2	SBA-15	4

Table S2. Thickness and cross-sectional area of the sample pellets investigated by electrochemical impedance spectroscopy.

	Sample	Pellet thickness (μm)	Cross-sectional area (cm^2)
Figure 2a	pristine $Na_2B_{12}H_{12}$	525	0.785
	nanostructured $Na_2B_{12}H_{12}$	244	0.785
	$Na_2B_{12}H_{12}$+25SiO_2	295	0.785
	$Na_2B_{12}H_{12}$+35SiO_2	342	0.785
	$Na_2B_{12}H_{12}$+40SiO_2	250	0.785
Figure 2b	$Na_2B_{12}H_{12}$+35SiO_2 1h	349	0.785
	$Na_2B_{12}H_{12}$+25SiO_2 2h	275	0.785
	$Na_2B_{12}H_{12}$+25SiO_2 3h	275	0.785
	$Na_2B_{12}H_{12}$+25SiO_2 3.5h	282	0.785
	$Na_2B_{12}H_{12}$+25SiO_2 4h	308	0.785
	$Na_2B_{12}H_{12}$+25SiO_2 4h	460	0.785
	$Na_2B_{12}H_{12}$+25SiO_2 8h	288	0.785
Figure 2c	$Na_2B_{12}H_{12}$+35SiO_2-A90	365	0.785
	$Na_2B_{12}H_{12}$+35SiO_2-A90	387	0.785
	$Na_2B_{12}H_{12}$+35SiO_2-A200	328	0.785
	$Na_2B_{12}H_{12}$+35SiO_2-A200	354	0.785
	$Na_2B_{12}H_{12}$+35SiO_2-A200	430	0.785
	$Na_2B_{12}H_{12}$+35SiO_2-A300	422	0.785
	$Na_2B_{12}H_{12}$+35SiO_2-A300	494	0.785
	$Na_2B_{12}H_{12}$+35SiO_2-A380	308	0.785
	$Na_2B_{12}H_{12}$+35SiO_2-A380	460	0.785
	$Na_2B_{12}H_{12}$+35SiO_2-SBA15	314	0.785
	$Na_2B_{12}H_{12}$+35SiO_2-SBA15	437	0.785

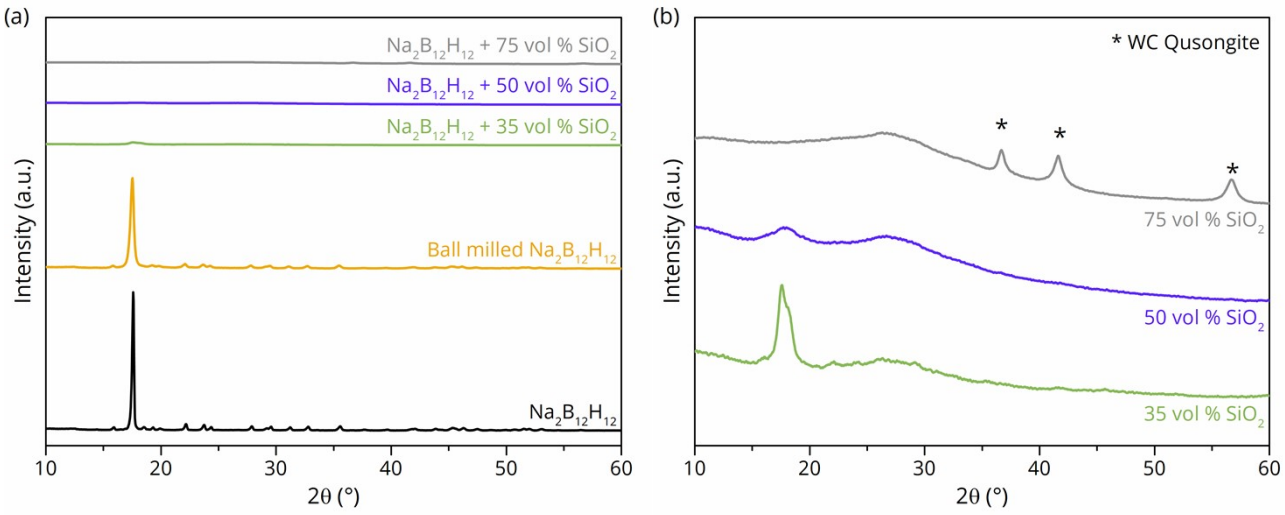

Figure S1. (a) Room-temperature X-ray diffractograms of pristine $Na_2B_{12}H_{12}$ before and after ball milling and $Na_2B_{12}H_{12}$-based nanocomposites. (b) X-ray diffractograms of $Na_2B_{12}H_{12}$-based nanocomposites containing varying amounts of SiO_2 (WC, PDF 00-051-0939).

Fig. S1a and b show that the broadening of the main diffraction peak of $Na_2B_{12}H_{12}$ in the nanocomposites increases with the SiO_2 content, due to amorphization and nanostructuring. Tungsten carbide (WC) impurities originating from the WC bowls and balls used for the mechanochemical milling, are observed at very high SiO_2 contents (75 vol %). This, interestingly, reveals that the softness of $Na_2B_{12}H_{12}$ prevents severe wearing of the milling equipment, as no crystalline WC is observed in high $Na_2B_{12}H_{12}$-containing nanocomposites used for assembling batteries.

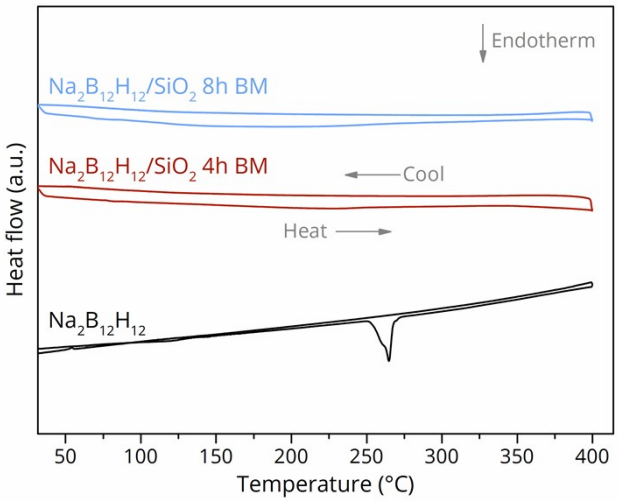

Figure S2. Differential scanning calorimetry analysis of pristine $Na_2B_{12}H_{12}$ and $Na_2B_{12}H_{12}$ + 35 vol % SiO_2 nanocomposites after 4h and 8h of mechanochemical treatment.

Differential scanning calorimetry measurements were performed in a Mettler Toledo HP DSC 1 with a PC10 pressure controller element in aluminium pans that allow for gas exchange. An argon pressure of p(Ar) = 2 bar and a flowrate = 10 ml min^{-1} were maintained, while heating and cooling the samples at a rate of 10 K min^{-1} and 5 K min^{-1}, respectively. A temperature-induced phase transition was observed for pristine $Na_2B_{12}H_{12}$. However, after ball milling with SiO_2 the solid-solid phase transition is absent, emphasizing the identified high degree of amorphization and the transformation of the low temperature phase.

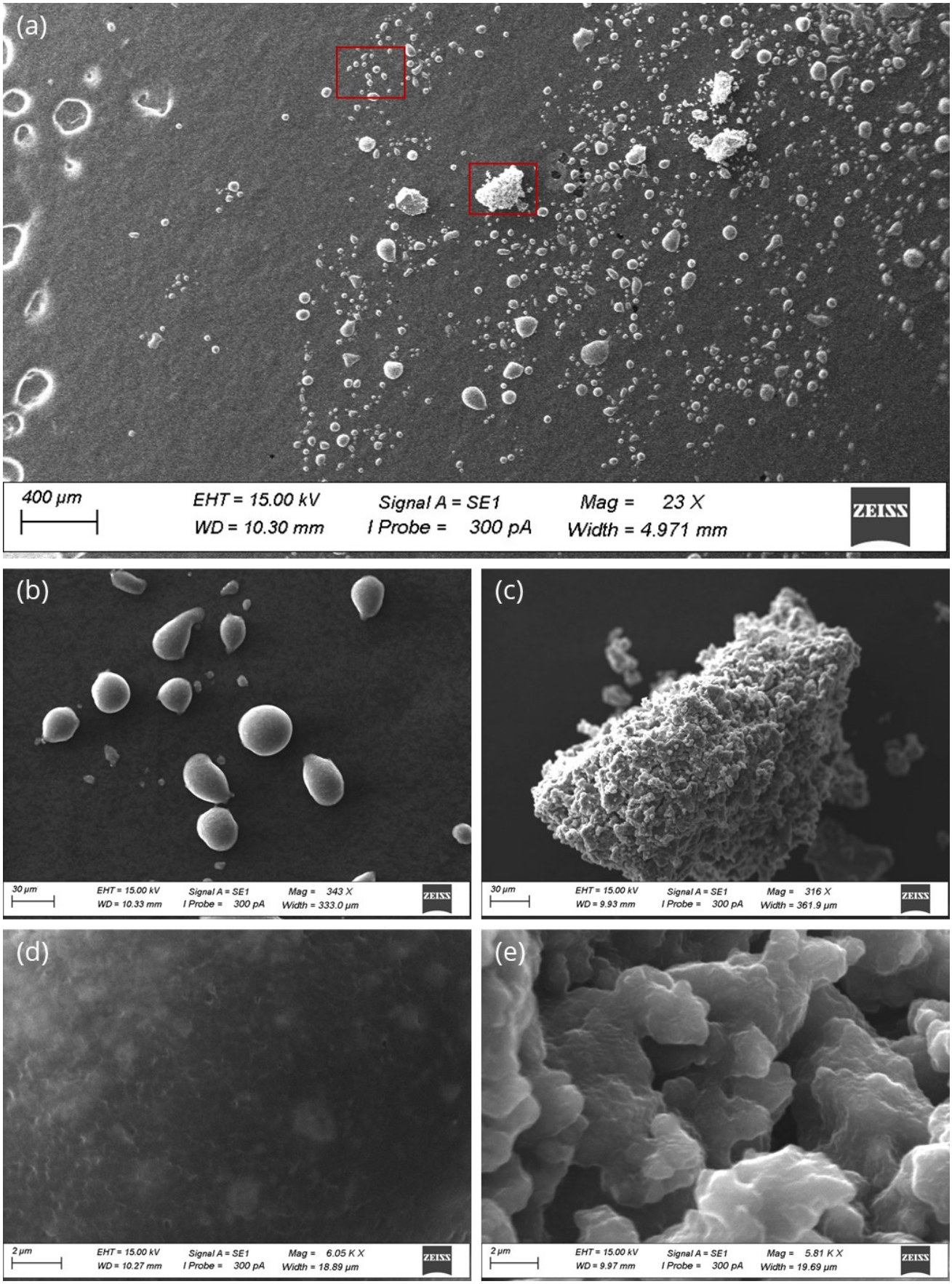

Figure S3. Scanning electron microscopy images of $Na_2B_{12}H_{12}$ + 35 vol % SiO_2-A200 after 4 h ball milling, illustrating the heterogeneous appearance within the nanocomposite. (a) Overview image, (b,d) high magnification images of the smooth particle domain and (c,e) high magnification images of the roughened agglomerate.

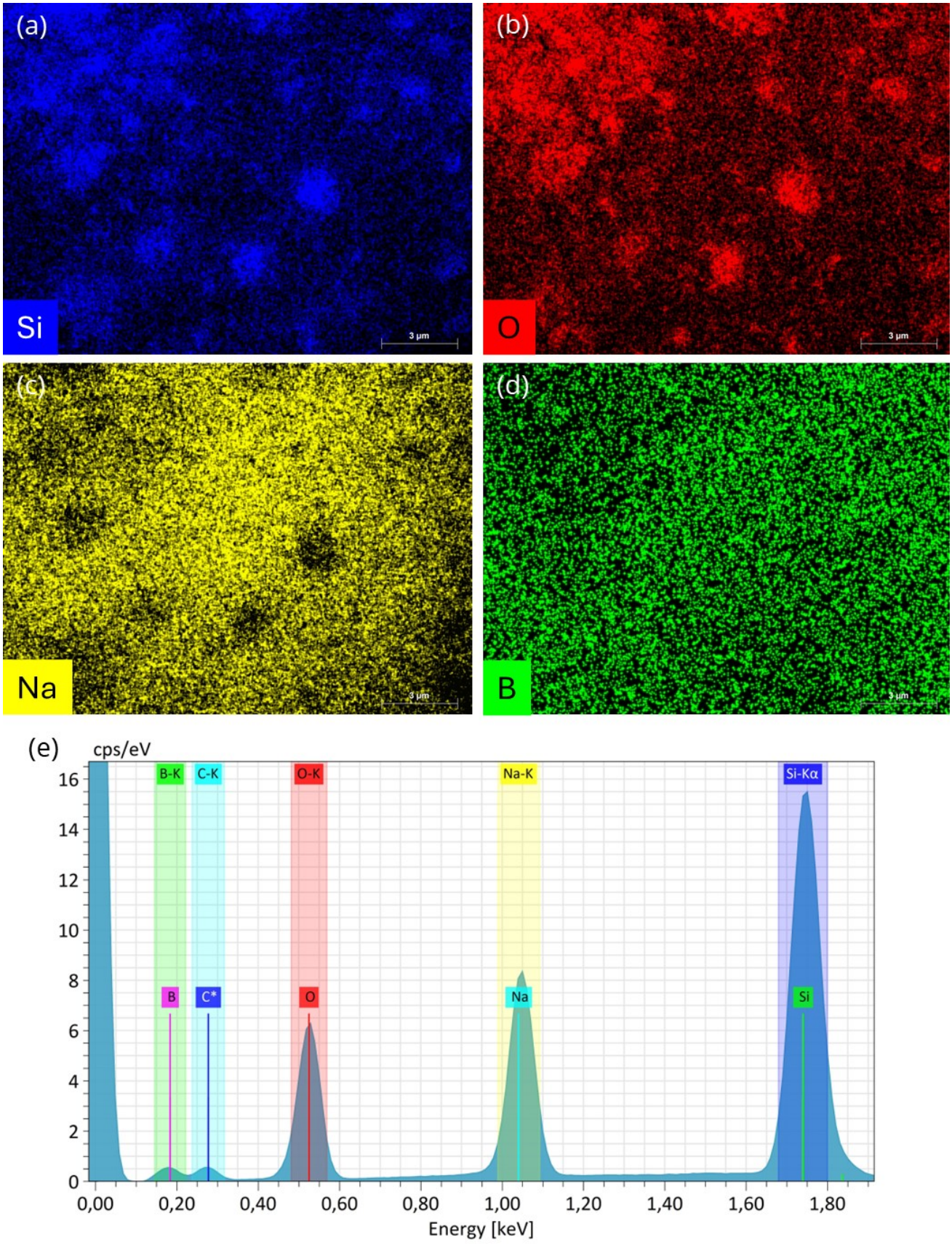

Figure S4. (a) Silicon, (b) oxygen, (c) sodium and (d) boron elemental maps of the high magnification scanning electron microscopy image of the smooth particle surface shown in Figure S2d. (e) Corresponding energy dispersive X-ray spectroscopy data.

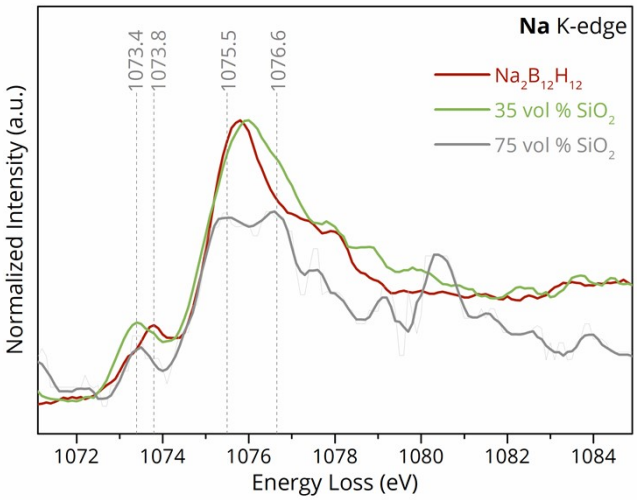

Figure S5. Sodium K-edge X-ray Raman scattering spectra of $Na_2B_{12}H_{12}$-based nanocomposites compared to pristine $Na_2B_{12}H_{12}$ for reference.

Due to a low signal to noise ratio in the Na K-edge region of the $Na_2B_{12}H_{12}$ + 75 vol % SiO_2 nanocomposite, a percentile filter was used for the data analysis.

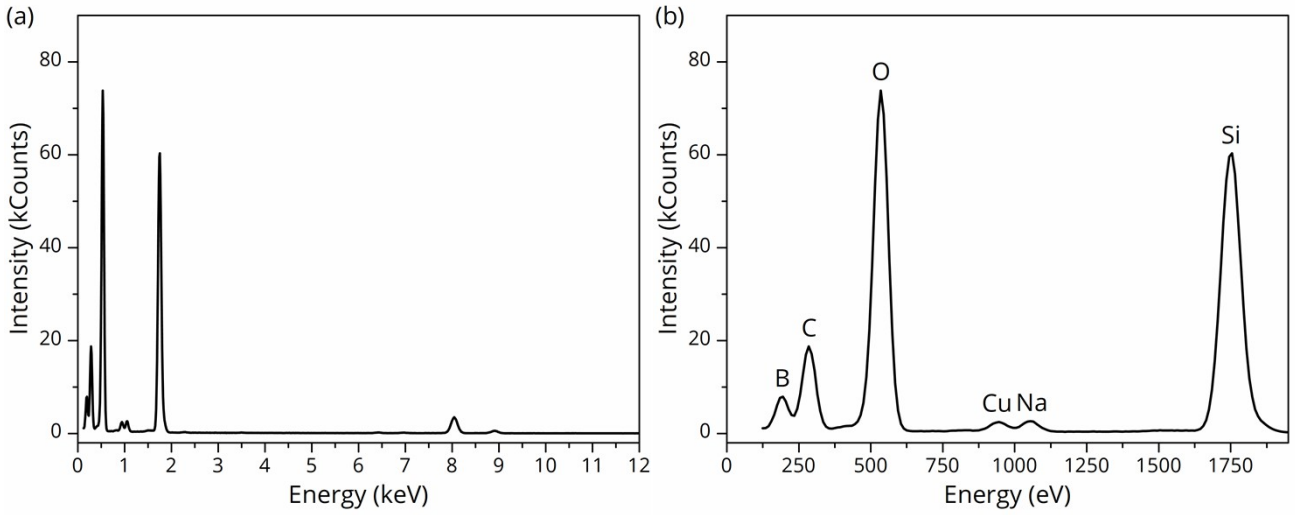

Figure S6. (a) Overview (b) expanded view of the energy dispersive X-ray spectroscopy data corresponding to the transmission electron microscopy image shown in Figure 5.

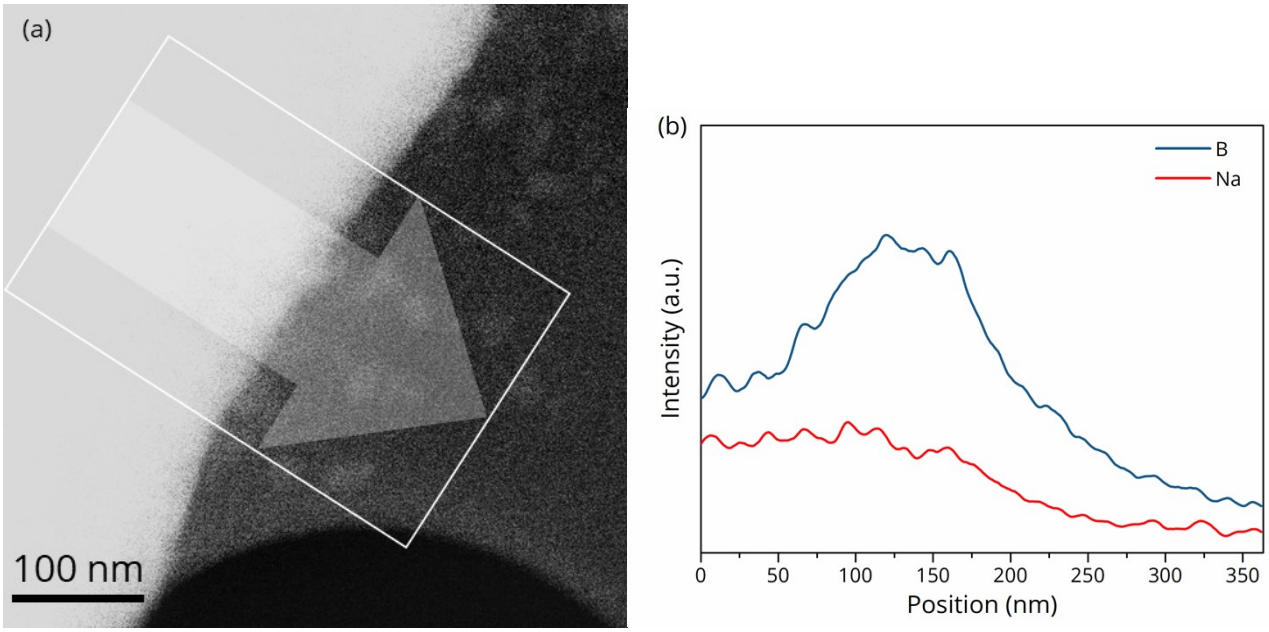

Figure S7. (a) Transmission electron microscopy image of $Na_2B_{12}H_{12}$+ 35 vol % SiO_2, with a visualization of the line scan area. (b) Energy dispersive X-ray spectroscopy line scan data.

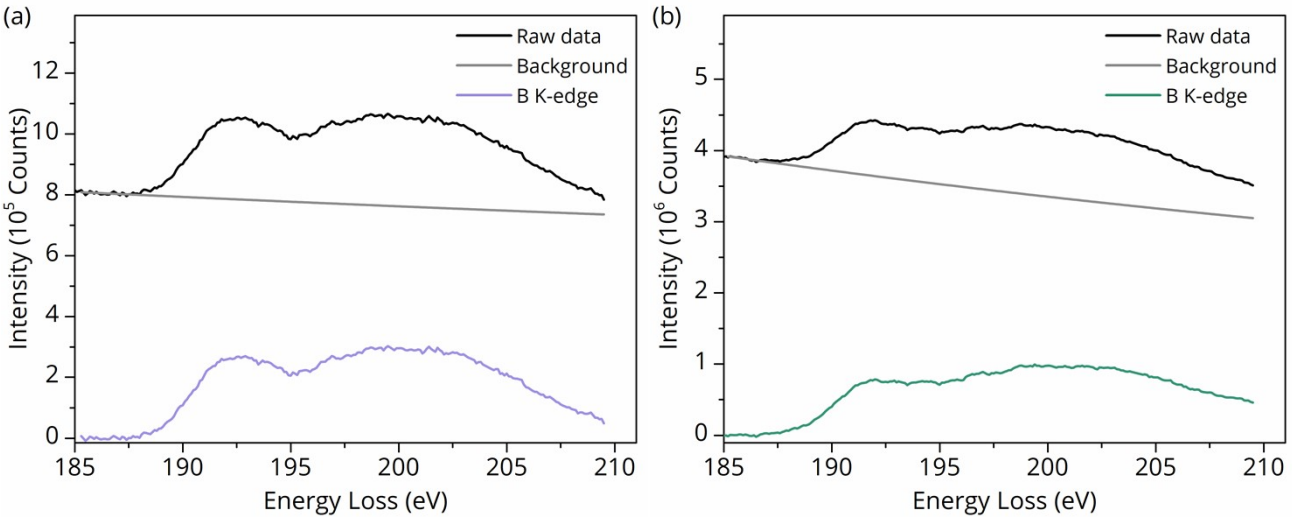

Figure S8. Raw and logarithmic-background corrected electron energy loss spectroscopy data of $Na_2B_{12}H_{12}$+ 35 vol % SiO_2 (a) in the surrounding and (b) at the surface of a SiO_2 agglomerate.

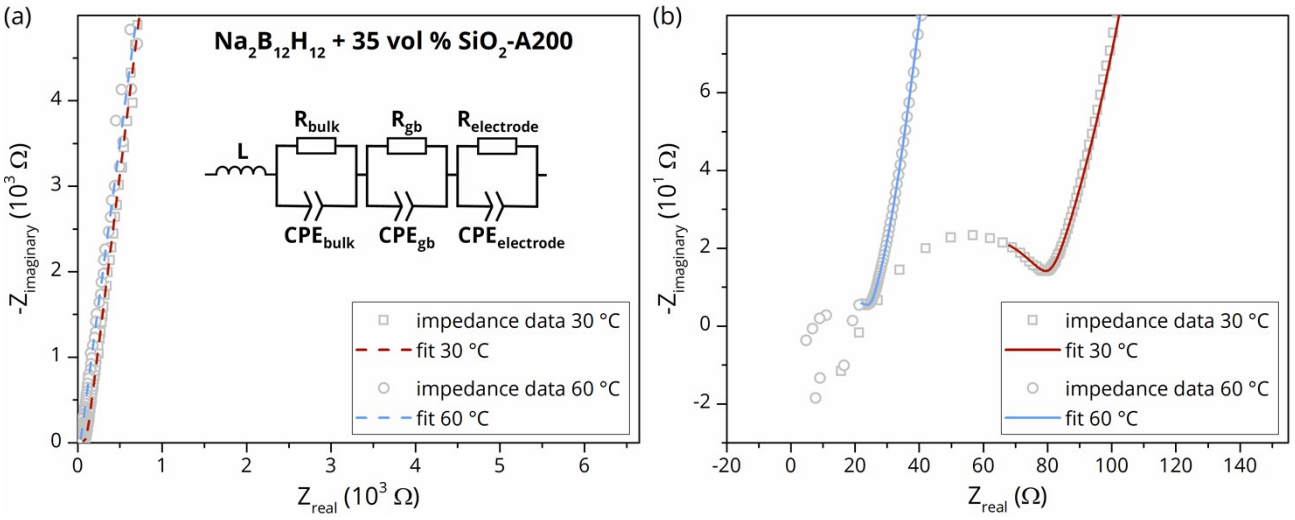

Figure S9. Nyquist representation of the electrochemical impedance spectroscopy data from $Na_2B_{12}H_{12}$+ 35 vol % SiO_2 after 4 h of ball milling (a) in the low frequency region, (b) in the high frequency region at 30 °C and 60 °C.

The electrolyte resistance $R_{electrolyte} = R_{bulk} + R_{gb}$, was extracted from the impedance data using the Python-based software DECiM.[1] Here, R_{bulk} represents the contribution of the bulk material, while R_{gb} could be assigned to the grain boundaries. In combination with the sample thickness L and the electrode area A, the conductivity was calculated using $\sigma = L \times (R_{electrolyte} \times A)^{-1}$. The activation energy (E_A) for an ion jump was obtained using the Arrhenius-type equation $\sigma T = \sigma_0 \exp(-E_A(RT)^{-1})$.[2]

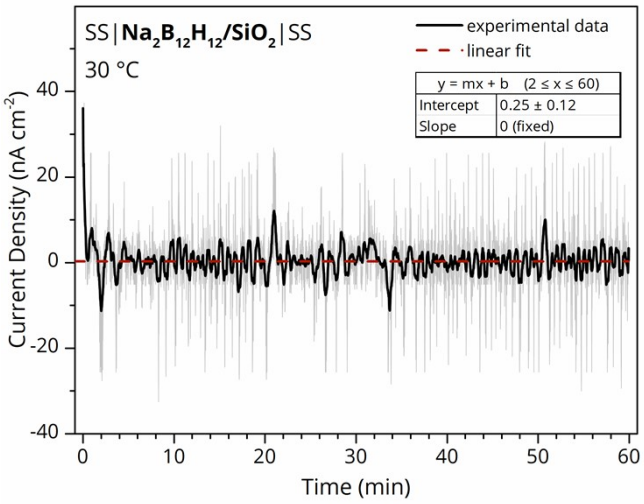

Figure S10. Chronoamperometry data (U = 0.5 V) of $Na_2B_{12}H_{12}$+ 35 vol % SiO_2 after 4 h of ball milling with blocking stainless steel (SS) electrodes. The table shows the linear fitting results. An average current density of 0.25 nA cm^{-2} for x ≥ 2 min was calculated, which is regarded as the resolution limit of the setup.

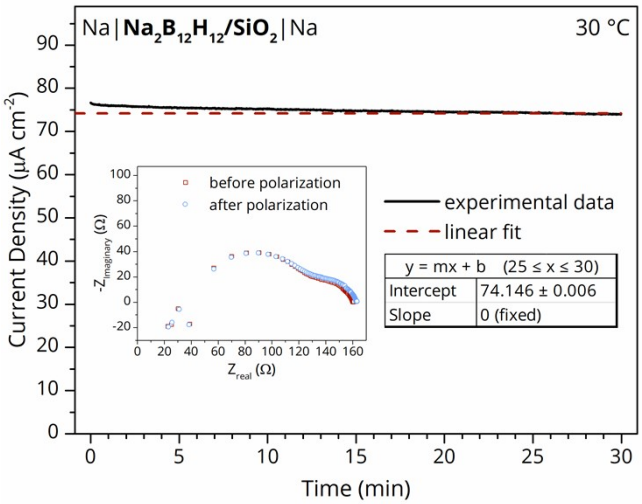

Figure S11. Chronoamperometry data (U = 10 mV) of $Na_2B_{12}H_{12}$+ 35 vol % SiO_2 after 4 h of ball milling with non-blocking sodium electrodes. The inset shows the impedance in Nyquist representation before and after the experiment. At x = 0 a current density of 76.7 μA cm^{-2} was measured, and for 25 ≤ x ≤ 30 min, a mean current density of 74.1 μA cm^{-2} was calculated.

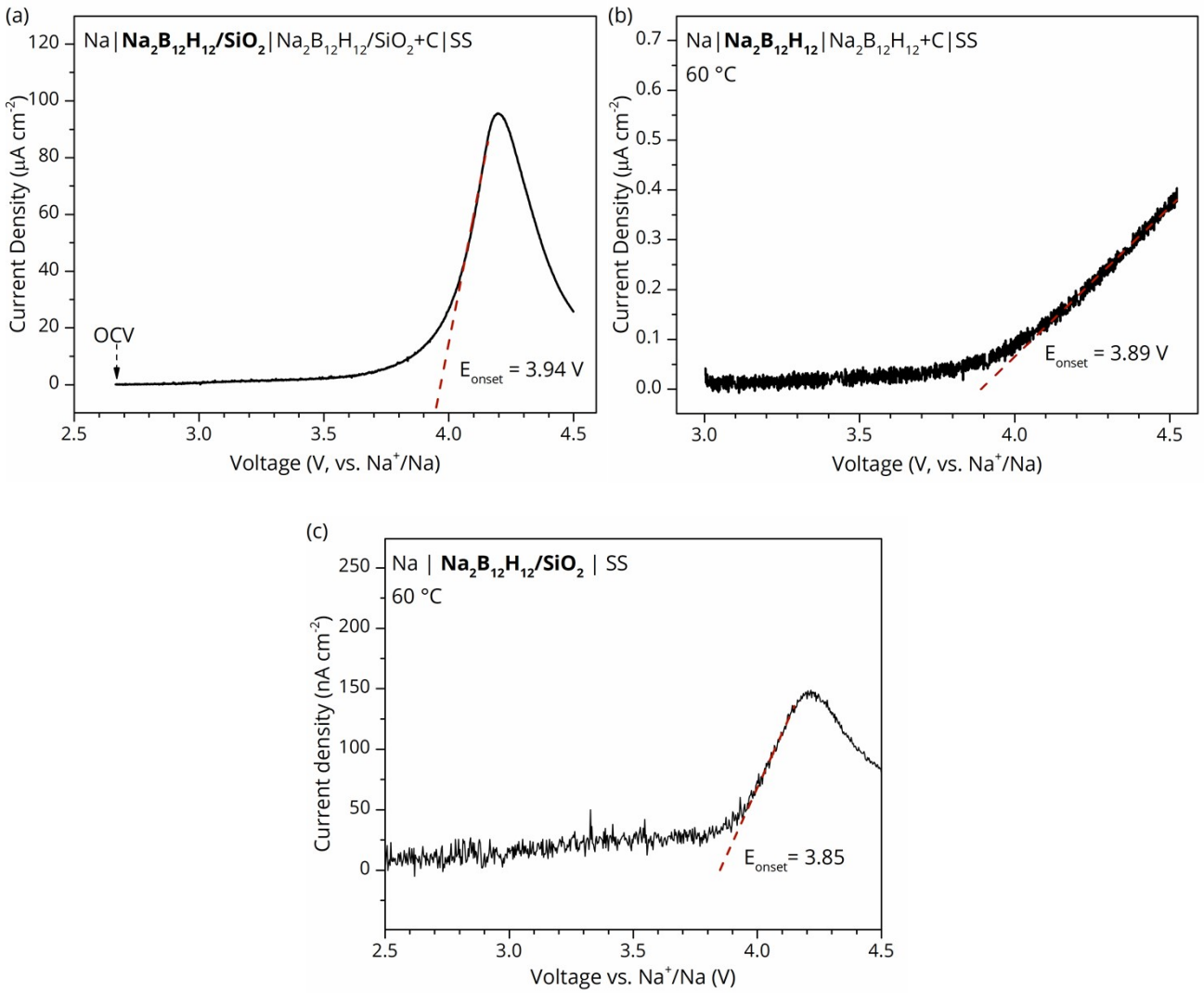

Figure S12. Linear sweep voltammetry of (a) $Na_2B_{12}H_{12}$ + 35 vol % SiO_2 and (b) pristine $Na_2B_{12}H_{12}$ with the addition of conductive carbon and (c) Linear sweep voltammetry of $Na_2B_{12}H_{12}$ + 35 vol % SiO_2 without the addition of carbon.

Cells for linear sweep voltammetry were assembled with a stainless steel working electrode and metallic sodium as counter and reference electrode. The contact area between the SSE and the working electrode was improved by compacting a mixture of carbon and SSE (5:95 weight ratio) on top of the SSE, resulting in a 2-layered pellet (Fig. S12a and b).[3] The sweep was carried out with a scan rate of 100 $\mu V\ s^{-1}$ after a rest period of 2 h. The onset voltage was extracted from the intersection of a linear fit to the steep current rise with the baseline, which was estimated to be zero to avoid overestimating the oxidative stability.

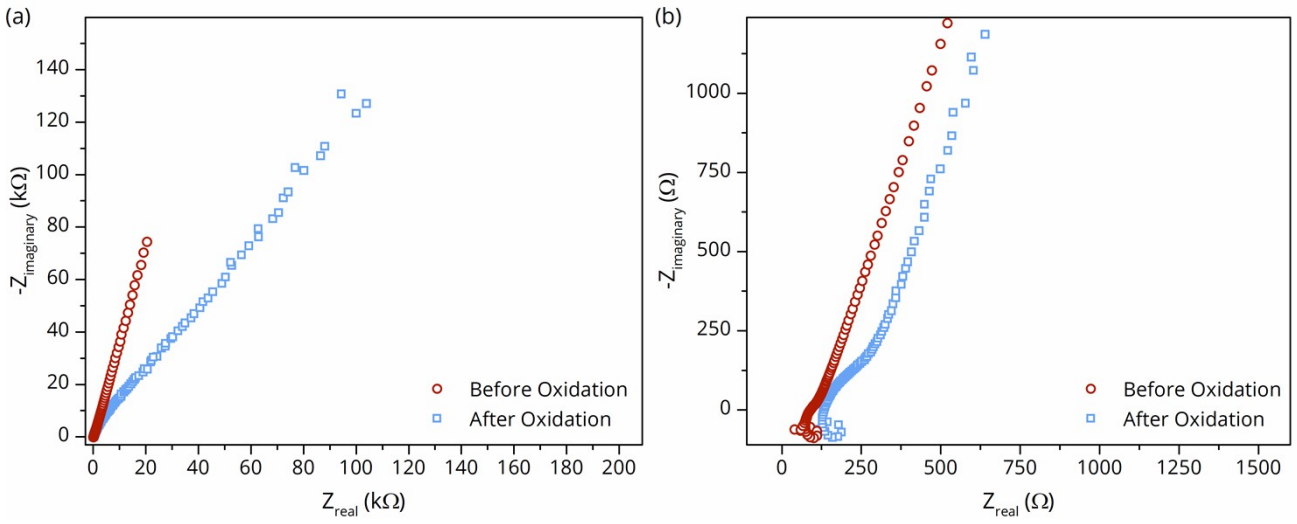

Figure S13. (a) Overview and (b) high frequency electrochemical impedance spectroscopy data of $Na_2B_{12}H_{12}$ + 35 vol % SiO_2 with sodium counter electrode before and after electrochemical oxidation at 60 °C.

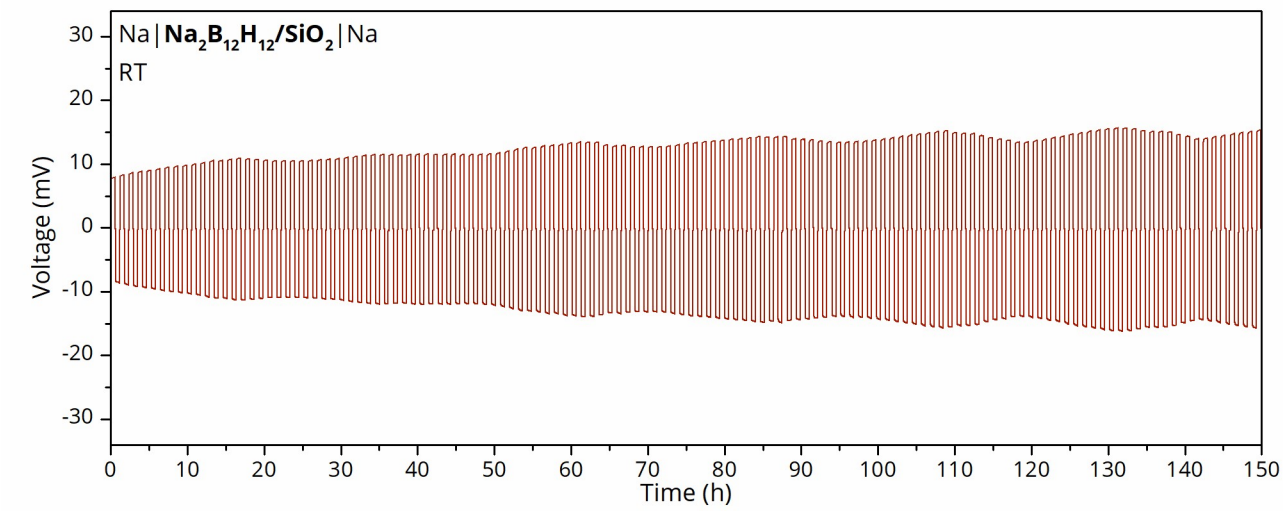

Figure S14. Chronopotentiometry data with an alternating constant current density of 0.05 mA cm^{-2}. For the measurement a $Na_2B_{12}H_{12}$+ 35 vol % SiO_2 solid-electrolyte was sandwiched between non-blocking sodium electrodes.

Minor voltage fluctuations in the chronopotentiometry data are likely due to the variations in room temperature between day and night.

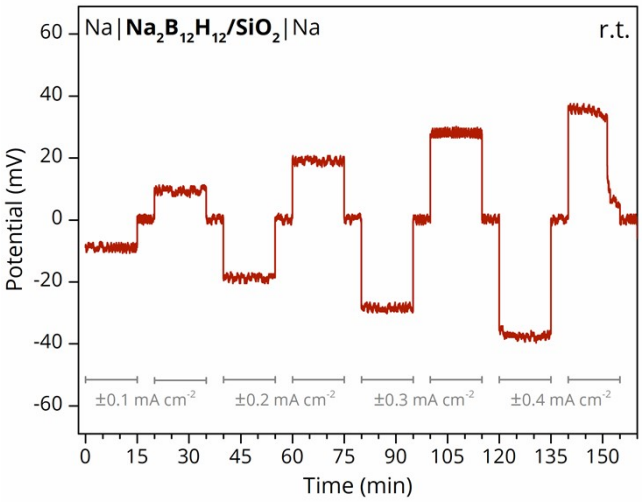

Figure S15. Chronopotentiometry data with increasing alternating current densities from $Na_2B_{12}H_{12}$+ 35 vol % SiO_2 solid-electrolyte and non-blocking sodium electrodes.

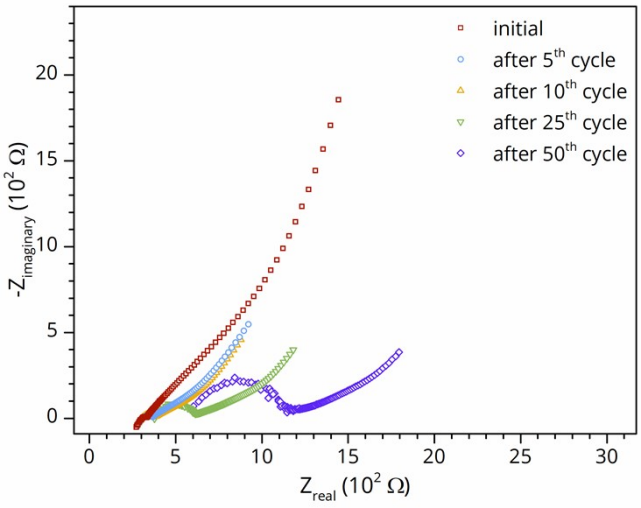

Figure S16. Nyquist representation of the electrochemical impedance spectroscopy data from the battery cell Na | $Na_2B_{12}H_{12}/SiO_2$ | $Na_2Mn[Fe(CN)_6]$ operated at 40 °C.

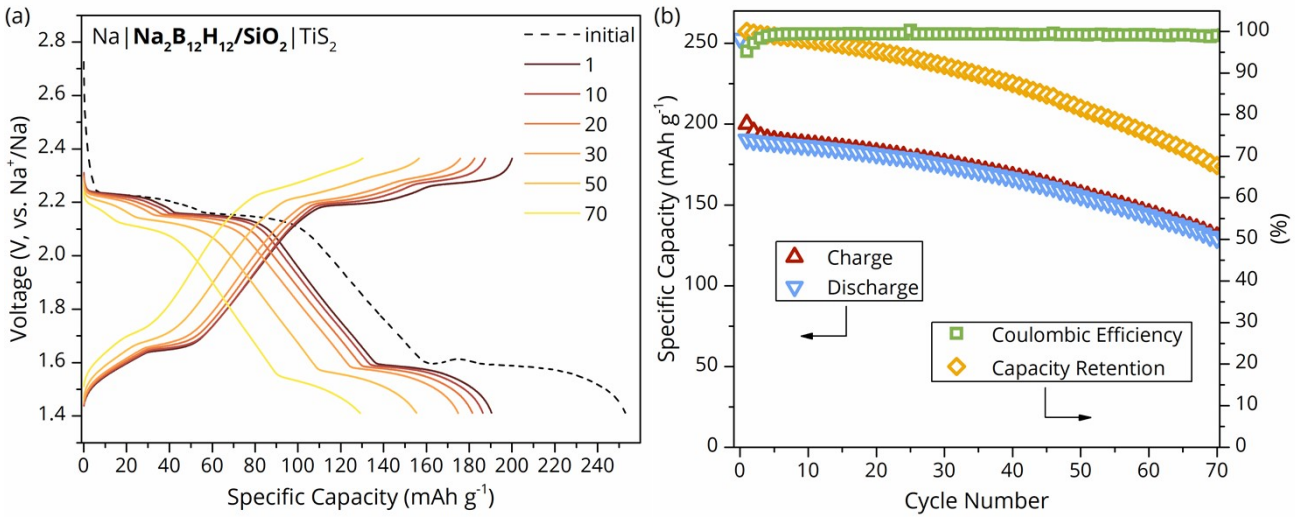

Figure S17. Battery performance of an all-solid-state battery (Na | $Na_2B_{12}H_{12}/SiO_2$ | TiS_2) operated at 60 °C with a charging/discharging rate of C/10 (38.04 μA cm^{-2}). (a) Galvanostatic cycling profile and (b) details about coulombic efficiency and capacity retention per cycle.

Battery cells employing TiS_2 as the cathode active material exhibit a pronounced initial capacity loss, followed by gradual capacity fading with increasing cycle number, which can be attributed to interfacial stability limitations with the electrode materials at an elevated temperature of 60 °C.[4]

References

1. H. P. Rodenburg and P. Ngene, *SoftwareX*, 2024, **27**, 101807.
2. R. J. D. Tilley, *Defects in Solids*, Wiley, Hoboken, N. J., 2008.
3. R. Asakura, L. Duchêne, R.-S. Kühnel, A. Remhof, H. Hagemann and C. Battaglia, *ACS Appl. Energy Mater.*, 2019, **2**, 6924–6930.
4. X.-W. Chen, J.-X. Kang, Z.-H. Fan, N. Zhang, W.-Y. Zhang, G.-G. Zhang, A.-Q. Zhu, Z.-W. Lu, P. Qiu, Y. Wu and X. Chen, *Small*, 2024, **20**, 2401439.